Hierarchical Decomposition and Deep Learning Forecasting for Operational Region Modeling of Flexibility Resources

Haiteng Han, Xiangchen Jiang, Zijian Zhou, Bin Shao, Simin Zhang, Chen Wu✉
School of Electrical and Power Engineering
Hohai University
Nanjing, China

***Abstract*—With the rapid integration of renewable energy sources into power systems, flexibility resources such as wind and photovoltaic (PV) generation introduce significant uncertainties that challenge traditional centralized dispatch strategies. This paper presents a hierarchical feature extraction and parallel forecasting framework for distributed flexibility resource regulation considering operational region constraints. The proposed strategy employs Seasonal-Trend decomposition using Loess (STL) and Variational Mode Decomposition (VMD) to extract multi-scale temporal features from power sequences, capturing both long-term trends and high-frequency disturbances. A parallel forecasting architecture combining Informer and Long Short-Term Memory (LSTM) models is developed to leverage global dependencies and local dynamics simultaneously. To quantify regulation capacity under physical constraints, the operational region theory is integrated to define feasible power regions in the active-reactive plane for wind, PV, and energy storage systems. Case studies demonstrate that the proposed strategy significantly improves forecasting accuracy and enhances flexibility utilization efficiency.**

***Index Terms*-- Flexibility resources, hierarchical decomposition, deep learning, operational region, renewable energy forecasting.**

I. INTRODUCTION

With the accelerating integration of renewable energy into modern power systems, flexibility resources such as wind and PV generation have become essential for grid regulation. However, their inherent stochasticity and intermittency introduce significant uncertainties that challenge the reliability of conventional centralized dispatching [1]. As the penetration of distributed resources increases, the mismatch between their rapid dynamic fluctuations and the limited responsiveness of traditional scheduling methods poses growing threats to grid security and operational stability [2].

In recent years, deep learning models have demonstrated strong potential in renewable energy forecasting. LSTM networks effectively capture short-term temporal dependencies [3], while Transformer-based architectures such as Informer leverage sparse self-attention mechanisms to model long-range sequential patterns [4]. Despite these advances, most existing studies focus on single time scales and employ a single model architecture, overlooking the inherent multi-scale temporal characteristics of power output series. In practice, these series contain not only long-term trends and periodic patterns driven by diurnal and seasonal cycles, but also high-frequency disturbances arising from meteorological variability such as wind gusts and cloud transients [5]. Neglecting these multi-scale features can lead to substantial forecasting errors, particularly during periods of rapid fluctuation, which in turn undermines the effectiveness of downstream scheduling decisions.

Time-series decomposition techniques offer a principled approach to address this challenge. STL separates a time series into trend, seasonal, and residual components, providing a structured representation of dominant temporal patterns [6]. VMD further decomposes non-stationary residual signals into band-limited intrinsic modes with distinct frequency characteristics [7]. Combining STL and VMD in a hierarchical framework enables comprehensive multi-scale feature extraction that neither method achieves alone.

For forecasting, Informer excels at capturing global dependencies in long sequences through its ProbSparse self-attention and information distilling mechanisms [8], yet it tends to smooth over localized short-term fluctuations. Conversely, LSTM is well suited for modeling local dynamic variations but suffers from gradient degradation in long sequences [9]. A single model thus finds it challenging to balance global and local temporal modeling simultaneously. Moreover, existing studies generally treat the forecasting and scheduling stages independently, with limited consideration of operational region constraints that define the physically feasible regulation space of flexibility resources [10].

To address these limitations, this paper proposes a regulation strategy for flexibility resources based on hierarchical decomposition and deep learning forecasting, with explicit integration of operational region constraints. The main contributions are summarized as follows:

This work was supported by the National Natural Science Foundation of China under Grant No. 52307090.

979-8-3315-8138-1

1) A two-layer STL-VMD decomposition framework is proposed to separate long-term trends, periodic patterns, and high-frequency disturbances from wind and PV power series, providing clearer multi-scale input features for forecasting.

2) A parallel Informer-LSTM architecture is developed with a consistency loss function to coordinate global dependency and local dynamic modeling, improving forecasting accuracy for complex non-stationary sequences.

3) The forecasting outputs are directly embedded into operational region constraint modeling based on convex hull theory, establishing a complete pipeline from feature extraction to power forecasting to scheduling optimization.

The rest of this paper is organized as follows. Section II presents the STL-VMD hierarchical decomposition method. Section III develops the parallel Informer-LSTM forecasting framework. Section IV establishes the regulation model considering operational region constraints. Section V provides case studies, and Section VI concludes.

II. Time-Series Feature Extraction Based on Hierarchical Decomposition

The decomposition in this work is organized along the temporal dimension, as wind and PV power outputs contain features at multiple time scales: slow-varying trends, regular periodic patterns, and rapid high-frequency fluctuations. STL is first applied to extract the trend and seasonal components, and VMD is then used to further decompose the non-stationary residual into distinct frequency modes.

A. Structural Time-Series Feature Extraction Based on STL

This paper employs STL as the first layer decomposition tool for extracting regulation potential features of flexibility resources. STL decomposes the original time series into three components: trend, seasonal, and residual:

$$y_t = T_t + S_t + R_t \tag{1}$$

where y_t represents the original observed value, T_t denotes the long-term trend, S_t represents the periodic fluctuation, and R_t is the random disturbance part after removing the trend and seasonality.

To further characterize the differential contributions of the trend, seasonal, and disturbance components to flexibility potential, the trend contribution ratio coefficient is introduced:

$$\eta_T = Var(T) / Var(y) \tag{2}$$

B. High-Frequency Decomposition via VMD

While STL effectively extracts trend and seasonal components, residuals still contain important information. To capture multi-scale structures, VMD is introduced as a complementary tool. In VMD, the residual is assumed to consist of several band-limited modes. Let the residual signal be $f(t)$, with mode set satisfying:

$$\sum_{k=1}^{K} u_k(t) = f(t) \tag{3}$$

To separate modes in the frequency domain, VMD employs spectral modulation and demodulation techniques. Each mode is converted to an analytic signal via Hilbert transform, then modulated by a complex exponential to shift its spectral center to near-zero frequency. Bandwidth is measured using the L2 norm of the demodulated signal's first derivative, where smaller bandwidth indicates more concentrated spectral energy and clearer frequency characteristics. The VMD optimization objective is:

$$\min_{\{u_k\},\{\omega_k\}} \sum_{k=1}^{K} \left\| \partial_t \left[u_k(t) \cdot e^{-j\omega_k t} \right]_2^2 \right\| \tag{4}$$

Through this optimization mechanism, VMD achieves a structured decomposition of the input signal's spectrum, presenting the residual sequence in modes with different frequency characteristics.

III. Parallel Forecasting of Flexibility Resources Regulation Potential

Informer is adopted for its ProbSparse self-attention mechanism that efficiently captures long-range dependencies, while LSTM is selected for its gating structure suited to short-term nonlinear dynamics. The parallel architecture combines their complementary strengths, offering advantages over classical methods that assume stationarity and single models that focus on only one temporal scale.

A. Long-Sequence Global Feature Forecasting via Informer

Given the high dimensionality and long time windows of distributed flexibility resource power series, this paper adopts the Transformer-based Informer model. Its ProbSparse Self-Attention mechanism significantly reduces computational complexity while maintaining strong modeling capability. The formal representation is [11]:

$$ProbSparseAttention(Q,K,V) = softmax\left(\bar{Q}K^T \big/ \sqrt{d}\right)V \tag{5}$$

Where Q, K and V represent the query, key, and value matrices, and $\bar{Q}$ represents the sparsified query matrix.

To capture multi-scale trends and periodic structures, Informer employs an information distilling mechanism in the encoder. This mechanism extracts multi-layer features through convolution and pooling operations, enhancing long-sequence representation and modeling efficiency:

$$X^{(l+1)} = MaxPooling\left(\sigma\left(Conv1d\left(X^{(l)}\right)\right)\right) \tag{6}$$

Where $X^{(l)}$ is the output of the l-th encoder layer, $Conv1d(\cdot)$ represents the one-dimensional convolution operation, $\sigma(\cdot)$ is the activation function, and $MaxPool1d(\cdot)$ is used for feature extraction.

B. Forecasting of Local Dynamic Features Based on LSTM

In this paper, LSTM is introduced to work in parallel with Informer, enhancing short-term disturbance capture and dynamic information extraction.

The LSTM input is the multi-scale feature sequence from decomposition, rather than raw power data, incorporating long-term trends, cyclic patterns, and high-frequency modes across multiple time scales. LSTM recursively processes this sequence, updating its memory cell and hidden state:

$$f_t = \sigma\left(W_f\left[h_{t-1}, x_t\right] + b_f\right); i_t = \sigma\left(W_i\left[h_{t-1}, x_t\right] + b_i\right) \tag{7}$$

$$\tilde{C}_t = \tanh\left(W_C\left[h_{t-1}, x_t\right] + b_C\right); C_t = f_t \odot C_{t-1} + i_t \odot \tilde{C}_t \tag{8}$$

$$o_t = \sigma\left(W_o\left[h_{t-1}, x_t\right] + b_o\right); h_t = o_t \odot \tanh\left(C_t\right) \tag{9}$$

Where f_t, i_t and o_t denote the forget, input, and output gates; h_{t-1} is the previous hidden state; C_t is the current cell state; W_C and b_C are network parameters. σ and $\odot$ denote sigmoid activation function and the Hadamard product.

C. Parallel Forecasting with Informer–LSTM

To capture multi-scale temporal features, Informer and LSTM are integrated in parallel. Informer extracts global dependencies from long sequences, while LSTM captures short-term dynamic fluctuations.

For efficient training, two separate outputs, $\hat{y}_t^I$ and $\hat{y}_t^L$, are generated, and the forecasting error is computed under the same objective:

$$\mathcal{L}_{\text{Informer}} = \frac{1}{N}\sum_{t=1}^{N}\left(y_t - \hat{y}_t^I\right)^2 ; \mathcal{L}_{LSTM} = \frac{1}{N}\sum_{t=1}^{N}\left(y_t - \hat{y}_t^L\right)^2 \quad (10)$$

A multi-scale consistency loss function is then employed for fused training:

$$\mathcal{L}_{\text{total}} = \alpha\mathcal{L}_{\text{Informer}} + (1-\alpha)\mathcal{L}_{LSTM} + \beta\left\|\hat{y}_{\text{Informer}} - \hat{y}_{LSTM}\right\|^2 \quad (11)$$

Where α is the weight coefficient, balancing global and local features, and β is the consistency constraint coefficient, which minimizes the difference between the outputs of the two models, ensuring consistency in trend and fluctuation layer forecasting.

IV. Flexibility Resource Adjustment Model Considering Operational Region Characteristics

After multi-scale extraction and forecasting, adjustment potential is transformed from raw data into meaningful feature sequences. Based on forecasting, operational region constructs a power adjustment envelope-based constraint structure, proposing a flexibility resource framework considering operational characteristics and uncertainties.

A. Two-Layer Framework for Distributed Flexibility Resource Regulation

This section develops a two-layer distributed flexibility resource adjustment framework that considers uncertainties: the upper layer is the risk management model, and the lower layer is the distributed flexibility adjustment model [6].

In the upper model, the operator achieves energy balance and economic optimization by setting trading prices with the microgrid. When the microgrid's power is imbalanced, the operator transacts with the higher-level grid. The operator sets a lower selling price $\pi_{i,t}^{\text{Ms}}$ and a higher buying price $\pi_{i,t}^{\text{Mb}}$, incentivizing the microgrid to optimize operation and reduce pressure on the higher-level grid. The optimization model is:

$$\max_{\pi_{i,t}^{\text{Mb}},\pi_{i,t}^{\text{Ms}},P_{i,t}^{\text{Mb}},P_{i,t}^{\text{Ms}}} \begin{pmatrix} \pi_t^{\text{Rs}}P_{i,t}^{\text{Ms}} - \pi_t^{\text{Rb}}P_{i,t}^{\text{Mb}} \\ +\pi_{i,t}^{\text{Mb}}P_{i,t}^{\text{Mb}} - \pi_{i,t}^{\text{Ms}}P_{i,t}^{\text{Ms}} \end{pmatrix} \quad (12)$$

$$\pi_{t,\min}^{\text{Mb}} \leqslant \pi_{i,t}^{\text{Mb}} \leqslant \pi_{t,\max}^{\text{Mb}} ; \pi_{t,\min}^{\text{Ms}} \leqslant \pi_{i,t}^{\text{Ms}} \leqslant \pi_{t,\max}^{\text{Ms}} \quad (13)$$

$$\sum_{t}^{\mathcal{T}}\pi_{i,t}^{\text{Mb}} / T \leqslant \pi_{i,t}^{\text{Mb},ave} ; \sum_{t}^{\mathcal{T}}\pi_{i,t}^{\text{Ms}} / T \geqslant \pi_{i,t}^{\text{Ms},ave} \quad (14)$$

Where π_t^{Rs} and π_t^{Rb} are the buying and selling prices between the operator and the higher-level grid, $P_{i,t,w}^{\text{Ms}}$ and $P_{i,t,w}^{\text{Mb}}$ represent the selling and buying power between the microgrid and the operator.

In the lower model, the microgrid, equipped with generation capability, can trade electrical energy with other microgrids or the operator.

$$P_{i,t}^{\text{Mb}}, P_{i,t}^{\text{Ms}} \in \arg\left\{\max\prod_{i=1}^{\mathcal{N}}\left(C_i^{\text{Non}} - \left(C_i^{\text{Tra}} + Ce_i^{\text{Pay}}\right)\right)^{\alpha_i}\right. \quad (15)$$

$$\begin{aligned} C_i^{\text{Non}}\left(\boldsymbol{x}_i^{\text{Non}}\right) &= \sum_{t=1}^{\mathcal{T}}\left[\pi_{i,t}^{\text{Mb}}P_{i,t}^{\text{Mb}} - \pi_{i,t}^{\text{Ms}}P_{i,t}^{\text{Ms}}\right] \\ C_i^{\text{Tra}}\left(\boldsymbol{x}_i^{\text{Tra}}\right) &= \sum_{t=1}^{\mathcal{T}}\left[\pi_{i,t}^{\text{Mb}}P_{i,t}^{\text{Mb}} - \pi_{i,t}^{\text{Ms}}P_{i,t}^{\text{Ms}}\right] \end{aligned} \quad (16)$$

$$P_{i,t}^{\text{Mb}} + P_{i,t}^{\text{Gen}} + P_{i,t}^{\text{trading}} + P_{i,t}^{\text{PV}} + P_{i,t}^{\text{Wind}} = P_{i,t}^{\text{Ms}} + P_{i,t}^{\text{load}} \quad (17)$$

$$0 \leqslant P_{i,t}^{\text{Mb}} \leqslant P_{i,\max}^{\text{Mb}} ; 0 \leqslant P_{i,t}^{\text{Ms}} \leqslant P_{i,\max}^{\text{Ms}} \quad (18)$$

$$0 \leqslant P_{i,t}^{\text{Wind}} \leqslant P_{i,\max}^{\text{Wind}} ; 0 \leqslant P_{i,t}^{\text{PV}} \leqslant P_{i,\max}^{\text{PV}} \quad (19)$$

$$\alpha_i = \sum_{t=1}^{\mathcal{T}}P_{i,t}^{\text{trading}} \Big/ \sum_{i=1}^{\mathcal{N}}\sum_{t=1}^{\mathcal{T}}P_{i,t}^{\text{trading}} ; \sum_{i=1}^{\mathcal{N}}\alpha_i = 1 \quad (20)$$

$$C_i^{\text{Tra}}\left(\boldsymbol{x}_i^{\text{Tra}}\right) + Ce_i^{\text{Pay}} \leqslant C_i^{\text{Non}}\left(\boldsymbol{x}_i^{\text{Non}}\right) ; \sum_{i=1}^{\mathcal{N}}Ce_i^{\text{Pay}} = 0 \quad (21)$$

B. Convex Hull-Based Operational Region

Assuming that the operational state of flexibility resources in the system at a given time is represented by the variable X, the feasible power space of its operational region can be defined as [12]:

$$\Omega = \left\{(P,Q) \mid \exists X, \text{s.t.} f_i(P,Q,X) \le 0, \forall i \in \mathcal{I}\right\} \quad (22)$$

Where f_i represents the operational constraints.

To determine operational region boundaries for each resource type, convex hull theory is applied. Given historical or simulation-generated data points $\left(P_k, Q_k\right)$, the operational region boundary is defined by their convex hull:

$$P = \sum_k \lambda_k P_k ; Q = \sum_k \lambda_k Q_k ; \sum_k \lambda_k = 1, \lambda_k \ge 0 \quad (23)$$

The weight coefficient λ_k ensures that the operating state falls within the convex region formed by the historical samples, thus defining the polygonal boundary of the operational region. The power adjustment capacity that the resource can provide is described by the following constraint:

$$P_{\min} \le P \le P_{\max} ; Q_{\min} \le Q \le Q_{\max} \quad (24)$$

Wind power regulation is limited by wind speed forecasting and the maximum output of the turbine, while reactive power regulation depends on the inverter capacity. The relationship must hold under all operating conditions:

$$0 \le P_{\text{wind}} \le P_{\text{wind}}^{\max} ; P_{\text{wind}}^2 + Q_{\text{wind}}^2 \le S_{\text{wind}}^2 \quad (25)$$

Where $P_{\text{wind}}^{\max}$ is the maximum available active power that the wind turbine can deliver at the current wind speed and S_{wind} is the rated capacity of the wind power inverter.

The operational region of PV generation is similarly constrained by inverter capacity and real-time factors such as sunlight and temperature. The active and reactive power of the PV system should satisfy the following constraints:

$$0 \le P_{\text{PV}} \le P_{\text{PV}}^{\max} ; P_{\text{PV}}^2 + Q_{\text{PV}}^2 \le S_{\text{PV}}^2 \quad (26)$$

Where $P_{\mathrm{PV}}^{\max}$ is the maximum available active power of the PV array, and S_{PV} is the rated inverter capacity.

When multiple types of flexibility resources are jointly involved in regulation, the overall operational region is determined by aggregating the operational regions of the individual resources:

$$\Omega_{total} = \left\{ (P,Q) \middle| (P,Q) = \sum_{i=1}^{n} \left(P_i, Q_i\right), \left(P_i, Q_i\right) \in \Omega_i \right\} \quad (27)$$

To account for forecast uncertainty, the operational region boundaries are conservatively contracted by 10% as a safety margin, ensuring a constraint violation rate below 3%.

V. Case Studies

The proposed framework is validated on a system comprising a grid operator with three generators (350/300/250 kW) and an alliance of three microgrids. Each microgrid is equipped with gas turbines (200/0/400 kW), PV units (150/200/130 kW), wind units (0/100/130 kW), and ESS (150/200/150 kW).

The wind and PV data are based on historical reanalysis datasets from the European Centre for Medium-Range Weather Forecasts (ECMWF) and the National Aeronautics and Space Administration (NASA), available at www.xihe-energy.com, covering one full year at 1-hour resolution (8,760 samples), split into 80%/20% for training/testing, with an input window of 168 hours and a horizon of 24 hours.

A. Analysis of Hierarchical Decomposition

Figure 1 illustrates the time-series data and STL decomposition results for various types of flexible resources.

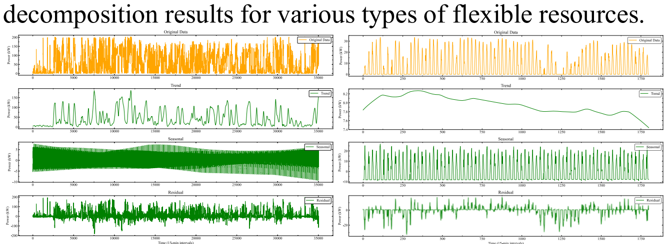

(a) (b)

Fig. 1. STL Decomposition Results of Wind and PV Time Series

Fig. 1(a) shows wind power decomposition: trend reflects long-term variations, seasonal shows daily cycles, and residual highlights high-frequency oscillations from wind disturbances, revealing short-term regulation capacity. Fig. 1(b) shows PV decomposition: trend represents irradiance changes, seasonal shows stable daily cycles, and residual captures short-term disturbances like cloud cover.

Since high-frequency non-stationary information remains in STL residuals, VMD is further applied for multimodal decomposition.

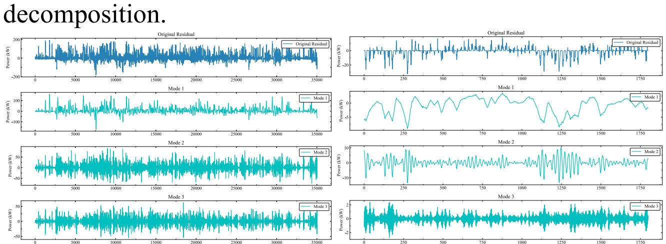

(a) (b)

Fig. 2. VMD Decomposition of Residuals

Fig. 2(a) shows VMD decomposition of wind power residuals. Mode 1 captures high-frequency spikes from gusts, Mode 2 reflects medium-frequency fluctuations, and Mode 3 reveals low-frequency trends. Fig. 2(b) shows PV residual decomposition. Mode 1 reflects high-frequency cloud disturbances, Mode 2 indicates medium-frequency variations, and Mode 3 captures low-frequency sunlight fluctuations.

B. Analysis of Forecasting Results

Fig. 3 shows the Informer-LSTM parallel forecasting performance after STL-VMD decomposition.

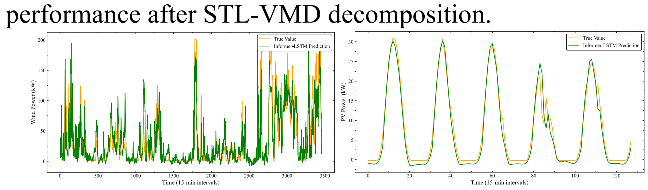

(a) (b)

Fig. 3. Wind and PV Power Forecasting Results

Fig. 3(a) presents wind power forecasting. The model tracks fluctuations well, with errors within acceptable ranges. Fig. 3(b) shows PV forecasting. While errors occur at peaks and troughs, the overall trend aligns well with data.

Fig. 4 displays forecasting results and training status for wind and PV after STL-VMD decomposition. MSE loss values for training and testing datasets reflect the model's convergence rate and fitting capability.

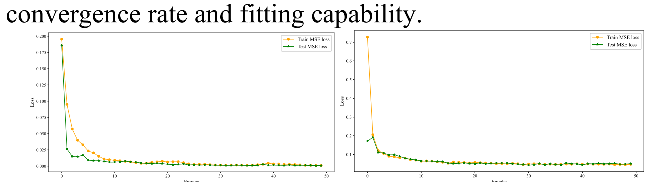

(a) (b)

Fig. 4. Model Training Convergence

Fig. 4(a) shows wind power training loss, which stabilizes after 20 epochs, indicating the model effectively captures local fluctuations and trends. Fig. 4(b) shows PV training loss, which decreases sharply after 10 epochs, demonstrating effective capture of periodic characteristics.

TABLE I. Forecasting Performance Comparison

Method	Wind (1h)	Wind (24h)	PV (1h)	PV (24h)
	MAE/RMSE	MAE/RMSE	MAE/RMSE	MAE/RMSE
Proposed	18.3/24.6	62.2/83.5	12.5/16.8	45.6/61.4
STL-VMD+Informer	23.2/30.8	65.8/88.9	15.8/21.4	49.7/67.2
STL-VMD+LSTM	20.5/27.4	74.3/99.7	14.3/19.2	55.8/75.4
STL+Informer-LSTM	21.8/29.2	68.3/91.7	14.2/19.1	50.2/67.9
VMD+Informer-LSTM	22.6/30.1	71.6/96.1	15.1/20.4	52.8/71.2
Informer-LSTM	26.4/35.3	78.5/105.3	17.8/24.0	58.4/78.7
Persistence	35.6/47.6	112.5/150.8	24.4/32.9	82.5/111.3

TABLE I presents the forecasting performance comparison. The proposed STL-VMD + Informer-LSTM achieves the best results across all scenarios, with overall MAPE of 4.82% for wind and 3.65% for PV. Compared with no decomposition, the 24h MAE is reduced by 20.8% for wind and 21.9% for PV. The parallel architecture outperforms single Informer by 5.5% and single LSTM by

16.3%, confirming the complementary advantages of both models.

C. Operating Region and Regulation Analysis

Fig. 5 presents the operating regions of flexibility resources constructed from predicted power, reflecting regulation capabilities, and providing boundary conditions for grid scheduling.

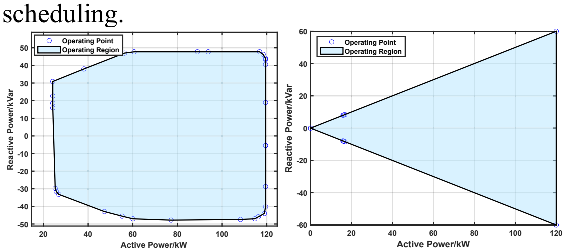

(a) (b)

Fig. 5. Operating Region of Renewable Resources

Fig. 5(a) shows the wind power operating region concentrated in the high active output region, with expanding boundaries at high output and narrowing at low output reflecting regulation constraints. Fig. 5(b) shows the PV region concentrated at high active power, with a converging low-power rgion indicating limited regulation under weak sunlight.

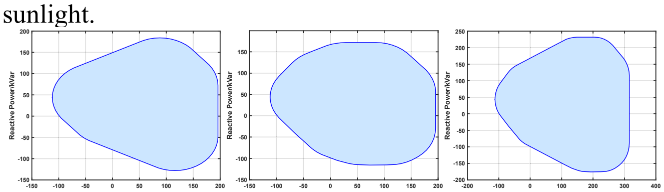

(a) (b) (c)

Fig. 6. Operating Regions of Microgrids

Fig. 6 shows microgrid scheduling operating regions, revealing distinct regulation characteristics. Microgrid 1 exhibits limited capability with points concentrated on the low-output supply side due to wind speed variations. Microgrid 2 demonstrates strong active and reactive regulation with a right-extended region. Microgrid 3 shows strong active power regulation reflected in its wide region.

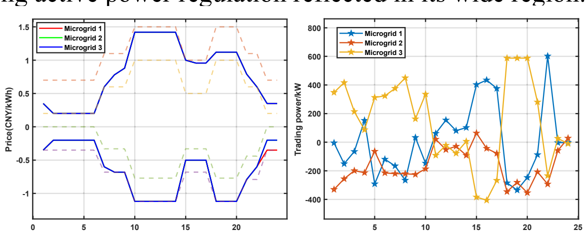

(a) (b)

Fig. 7. Trading prices and collaborative transactions among microgrids

Fig. 7 presents microgrid scheduling uder operational region constraints. Microgrid 3 operates near price limits due to near-saturation flexibility resources, while Microgrids 1 and 2 maintain stable mid-range prices. Constraints yield smoother inter-microgrid power exchange with reduced volatility, where Microgrid 1 operates within ±400kW, Microgrid 2 shows minimal fluctuations, and Microgrid 3 exhibits active trading reflecting abundant resources.

VI. Conclusion

This paper proposes a dynamic evaluation and optimal scheduling strategy for flexibility resources, based on hierarchical feature extraction and deep learning. By combining the STL and VMD to extract multilevel temporal features and utilizing the parallel Informer and LSTM models, the accuracy of forecasting for complex, non-stationary time series is enhanced. Additionally, by integrating the theory of operating regions, the proposed optimal scheduling model fully accounts for the physical constraints of flexible resources and grid security, ensuring both the stability and efficient operation of the grid. This study provides a feasible solution for optimizing grid scheduling in future scenarios with high renewable energy penetration.

Future work will focus on extending the framework to larger-scale power systems with more diverse flexibility resources and investigating real-time implementation strategies to further enhance practical applicability.

References

[1] Z. Liu, Z. Li, X. Jin, and H. Jia, "Multi-Time-Domain Hierarchical Scheduling of Integrated Energy Systems With Frequency Decomposition Considering Large-Scale Grid Connection of Electric Vehicles," *IEEE Trans. Smart Grid*, vol. 17, no. 1, pp. 244–254, Jan. 2026.

[2] X. Lin, X. Chen, Z. Chen, and L. Xie, "Stochastic model predictive control strategy with short-term forecast optimal SOC for a plug-in hybrid electric vehicle," *IEEE Trans. Transport. Electrific.*, vol. 10, no. 4, pp. 8685–8697, Dec. 2024.

[3] H. Zang *et al.*, "Distribution network optimization based on topology security-constrained integrated reinforcement learning," *Prot. Control Mod. Power Syst.*, 2025.

[4] J. Yang, N. Zhao, J. Wang, and Z. Wang, "Performance evaluation and optimization of solar-driven methane steam reforming and regression prediction analysis combined with data augmentation," *Renewable Energy*, vol. 256, p. 124471, Jan. 2026.

[5] Z. Yin, J. Wang, F. Yuan, and Z. Ma, "Collaborative data reconstruction and power prediction of wind turbine clusters," *Energy*, vol. 326, p. 136354, Jul. 2025.

[6] H. Han *et al.*, "Multi-stage optimization of community microgrid considering fair allocation and risk management," *J. Mod. Power Syst. Clean Energy*, 2025.

[7] J. Zhu, Y. Miao, H. Dong, S. Li, Z. Chen, and D. Zhang, "Short-term residential load forecasting based on K-shape clustering and domain adversarial transfer network," *J. Mod Power Syst. Clean Energy*, vol. 12, no. 4, pp. 1239–1249, 2024.

[8] D. Peng, Y. Liu, D. Wang, L. Luo, H. Zhao, and B. Qu, "Short-term PV-wind forecasting of large-scale regional site clusters based on FCM clustering and hybrid inception-ResNet embedded with informer," *Energy Conversion and Management*, vol. 320, p. 118992, Nov. 2024.

[9] J. Cheng, S. Jin, Z. Zheng, K. Hu, L. Yin, and Y. Wang, "Energy consumption prediction for water-based thermal energy storage systems using an attention-based TCN-LSTM model," *Sustainable Cities and Society*, vol. 126, p. 106383, May 2025, doi: 10.1016/j.scs.2025.106383.

[10] T. Zhou, D. Wang, H. Jia, J. Xiao, Y. Li, and H. Cheng, "The work region and total work capability of integrated energy system: Concepts, models, and mechanisms," *Applied Energy*, vol. 394, p. 126032, Sep. 2025.

[11] X. Yang, L. Yang, Y. Li, Z. Zhao, and Y. Zhang, "A new method of photovoltaic clusters power prediction based on informer considering time-frequency analysis and convergence effect," *Electric Power Systems Research*, vol. 238, p. 111049, Jan. 2025.

[12] M. Zhou, S. Chen, K. Huang, J. Liang, M. Fu, and G. Sun, "Coordination of medium-voltage distribution networks and microgrids based on an aggregate flexibility region approach," *Sustainable Energy, Grids and Networks*, vol. 39, p. 101485, Sep. 2024.

979-8-3315-8138-1